Geophys. J. Int. (2006) **164,** 109–124 doi: 10.1111/j.1365-246X.2005.02809.x

Seismogenic zone structure beneath the Nicoya Peninsula, Costa Rica, from three-dimensional local earthquake *P*- and *S*-wave tomography

Heather R. DeShon,[1]* Susan Y. Schwartz, Andrew V. Newman,[2] Victor González,[3] Marino Protti,[3] LeRoy M. Dorman,[4] Timothy H. Dixon,[5] Daniel E. Sampson[1] and Ernst R. Flueh[6]

[1] *University of California-Santa Cruz, Earth Sciences Department & IGPP, Santa Cruz, California, USA*
[2] *Georgia Institute of Technology, Atlanta, Georgia, USA*
[3] *Observatorio Vulcanológico y Sismológico de Costa Rica-UNA, Heredia, Costa Rica*
[4] *University of California-San Diego, Scripps Institution of Oceanography, La Jolla, California, USA*
[5] *University of Miami, Rosenstiel School of Marine and Atmospheric Science, Miami, Florida, USA*
[6] *IFM-GEOMAR and* SFB574, *Kiel, Germany*

Accepted 2005 September 21. Received 2005 September 6; in original form 2004 October 14

SUMMARY

The subduction plate interface along the Nicoya Peninsula, Costa Rica, generates damaging large ($M_w > 7.5$) earthquakes. We present hypocenters and 3-D seismic velocity models (V_P and V_P/V_S) calculated using simultaneous inversion of *P*- and *S*-wave arrival time data recorded from small magnitude, local earthquakes to elucidate seismogenic zone structure. In this region, interseismic cycle microseismicity does not uniquely define the potential rupture extent of large earthquakes. Plate interface microseismicity extends from 12 to 26 and from 17 to 28 km below sea level beneath the southern and northern Nicoya Peninsula, respectively. Microseismicity offset across the plate suture of East Pacific Rise-derived and Cocos-Nazca Spreading Center-derived oceanic lithosphere is ∼5 km, revising earlier estimates suggesting ∼10 km of offset. Interplate seismicity begins downdip of increased locking along the plate interface imaged using GPS and a region of low V_P along the plate interface. The downdip edge of plate interface microseismicity occurs updip of the oceanic slab and continental Moho intersection, possibly due to the onset of ductile behaviour. Slow forearc mantle wedge *P*-wave velocities suggest 20–30 per cent serpentinization across the Nicoya Peninsula region while calculated V_P/V_S values suggest 0–10 per cent serpentinization. Interpretation of V_P/V_S resolution at depth is complicated however due to ray path distribution. We posit that the forearc mantle wedge is regionally serpentinized but may still be able to sustain rupture during the largest seismogenic zone earthquakes.

Key words: Costa Rica, earthquake location, microseismicity, Middle America subduction zone, seismic velocities, tomography.

1 INTRODUCTION

Underthrusting earthquakes occurring along subduction megathrusts account for greater than 80 per cent of the seismic moment released worldwide (Pacheco & Sykes 1992). Great ($M_w > 8.0$), large ($M_w > 7$), and tsunamigenic earthquakes at convergent margins cause much damage and loss of life along heavily populated coastal zones. Understanding how and where seismogenic zone earthquakes occur is a major focus of the international scientific community. Recently, studies along the Middle America subduction zone offshore Costa Rica–Nicaragua have led to new insights into the complex interactions of thermal, mechanical, hydrological and compositional processes generating seismogenic zone seismicity.

Images of regional seismicity within the Middle America subduction zone in northern Costa Rica have been limited in the past by the spatial coverage of available permanent networks of single-component short-period seismometers. Earthquakes reported through country-wide catalogues by Observatorio Vulcanológico y Sismológico-Universidad Nacional de Costa Rica (OVSICORI-UNA) and the Red Sismológico Nacional (RSN-ICE) have relatively

*Now at: University of Wisconsin-Madison, Department of Geology and Geophysics, 1215 W. Dayton St., Madison, WI 53706, USA. E-mail: hdeshon@geology.wisc.edu

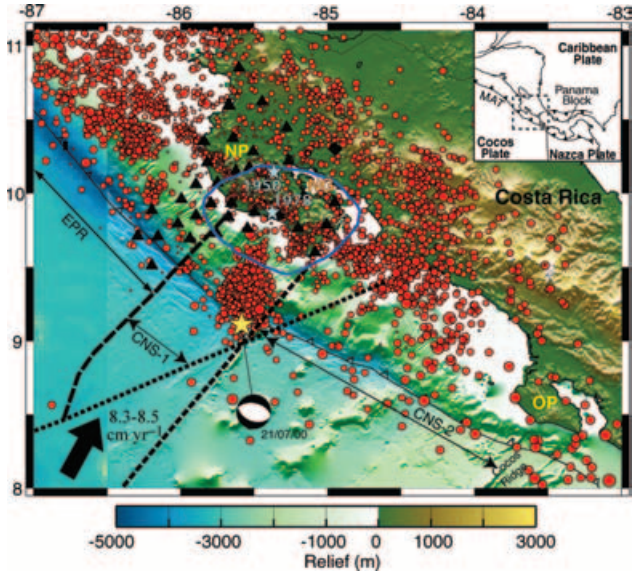

Figure 1. Overview map of the Nicoya CRSEIZE experiment. Cocos Plate oceanic crust formed at the East Pacific Rise (EPR) and at the Cocos-Nazca Spreading Center (CNS-1 and CSN-2) (Barckhausen *et al.* 1998, 2001) subducts along the Middle America Trench (MAT) offshore northern Costa Rica. The EPR–CNS plate suture occurs along a triple junction trace (bold long dashed line); other tectonic boundaries include a propagator trace (short dashed line) and a ridge jump (dotted line). Initial database locations using 1-D IASP91 velocity model are scaled by local magnitude (red circles). The Nicoya Experiment recorded interseismic seismogenic zone seismicity, crustal seismicity and the main shock and aftershock sequence of the 2000 Nicoya earthquake along the outer rise (yellow star with Harvard Centroid Moment Tensor solution). The M_w 7.7 1950 and M_w 6.9 1978 earthquakes (blue stars) and the 1950 aftershock region (blue line) provide one seismogenic zone estimate (Avants *et al.* 2001). NP: Nicoya Peninsula; NG: Nicoya Gulf; and OP: Osa Peninsula. Bathymetry is from von Huene *et al.* (2000).

large depth errors (>5 km), especially for those events occurring north and west of the primary networks (Quintero & Kissling 2001). Increased station coverage using temporary three-component seismometers on land and offshore the Nicoya Peninsula significantly improved the resolution of microseismicity along the shallow plate interface (Newman *et al.* 2002; DeShon & Schwartz 2004). The Nicoya Peninsula passive array component of the Costa Rica Seismogenic Zone Experiment (CRSEIZE) consisted of 20 short-period and broad-band seismometers that recorded across the peninsula from 1999 December to 2001 June and 14 broad-band ocean bottom seismometers (OBS) that recorded from 1999 December to 2000 June (Fig. 1). OBS were improved versions of those describe in Sauter *et al.* (1990) and Jacobson *et al.* (1991). The array recorded over 10 000 earthquakes, and analyst-reviewed *P*- and *S*-wave arrival times exist for ∼2000 local events. This extensive data set and station distribution allows for improved accuracy of earthquake locations with significantly reduced depth errors.

In this study *P*-wave arrival time and *S*–*P* traveltime delays recorded by the CRSEIZE Nicoya Peninsula seismic array are inverted to solve for best fitting hypocenters, station corrections and compressional and shear wave velocities. The resulting 3-D seismic velocity information is combined with the improved precision relocations of subduction-related seismicity to constrain material properties beneath the Nicoya Peninsula, Costa Rica. Study goals include:

(1) characterizing the geometric range of seismic activity within the subduction zone,

(2) correlating variations in seismicity to velocity structure near the plate interface and

(3) comparing the up- and downdip limits of seismogenic zone seismicity to available thermal models and physical properties of the dècollement.

2 GEOLOGIC AND TECTONIC SETTING

Oceanic Cocos Plate subducts beneath continental Caribbean Plate offshore northern Costa Rica at 83–85 mm yr^{-1}, 20° counterclockwise to orthogonal subduction at the Middle America Trench (MAT) (Fig. 1) (DeMets 2001). Coastal subsidence and uplift along the central coast range and the Nicoya Gulf are consistent with trench-normal locking along the plate interface (e.g. Marshall & Anderson 1995). Lundgren *et al.* (1999), Iinuma *et al.* (2004), and Norabuena *et al.* (2004) have inverted GPS site velocities to obtain estimates of interseismic locking along the plate interface beneath the peninsula. Norabuena *et al.* (2004), using data collected as part of CRSEIZE, found a component of along-strike crustal sliver transport and a variably coupled trench-normal plate interface, with strongest locking occurring at 14 ± 2 and 38 ± 2 km depth below sea level (BSL), updip and downdip of interseismic interplate seismicity. The resolution of the GPS inversion, however, precluded examination of along-strike variability in locking beyond the Nicoya Peninsula.

Seismic potential for the Nicoya Peninsula region has been estimated based on the rupture limits of the 1950 M_w 7.7 underthrusting earthquake and consideration of regional seismicity and plate coupling (Fig. 1) (Güendel 1986; Protti *et al.* 2001). The most recent damaging earthquake occurred on 1978 August 23 (Fig. 1). This M_w 6.9 earthquake, originally located offshore the peninsula at 25.7 km depth by Güendel (1986), had a focal mechanism consistent with thrusting along the plate interface, but comparison of the original hypocenter to the plate interface defined by refraction data (Christeson *et al.* 1999; Sallarès *et al.* 1999) places the earthquake within the oceanic crust. Avants *et al.* (2001) relocated both the 1950 and 1978 earthquakes reported by Güendel (1986) relative to the 1990 M_w 7.0 Nicoya Gulf earthquake (Protti *et al.* 1995b). These relocations place the older earthquakes slightly inboard and south of the original locations, more consistent with rupture along the plate interface (Fig. 1) (Avants *et al.* 2001). We assume consistent mislocation of these main shocks due to station geometry and propagation path errors and accordingly adjust the 1950 aftershock area, which was originally defined by Güendel (1986) using arrivals from a local temporary network. This provides a revised estimate of the potential seismogenic zone rupture along the Nicoya seismic gap (Fig. 1).

Though the bathymetry of the incoming Cocos Plate near the Nicoya Peninsula appears uniformly smooth seaward of the trench, it exhibits variability in lithospheric history and shallow thermal structure (e.g. Shipley *et al.* 1992; Kimura *et al.* 1997; Spinelli & Underwood 2004). Oceanic lithosphere subducting beneath the peninsula derives from both the Cocos-Nazca Spreading Center (CNS) and East Pacific Rise (EPR) (Fig. 1) (Barckhausen *et al.* 2001). Lithosphere formed at the CNS between 21.5 and 23 Ma subducts beneath the southern Nicoya Peninsula while lithosphere formed at the EPR subducts in the north. At the MAT, there is an ∼1 Ma age difference between the two lithospheres that corresponds

to a small (∼200 m offset) fracture zone (Walther & Flueh 2002). Due to hydrothermal circulation, heat flow through EPR crust is anomalously low (20–40 mW m^{-2}) compared to conductive cooling models (100 mW m^{-2}) (Stein & Stein 1992; Langseth & Silver 1996; Harris & Wang 2002; Fisher *et al.* 2003). However, CNS crustal heat flow is largely consistent with conductive cooling models (∼105–115 mW m^{-2}). The separation between hydrothermally cooled and normal oceanic crust follows a meandering pattern on the EPR crust and correlates to the plate suture at the MAT (Fisher *et al.* 2003; Hutnak 2006).

Current estimates of crustal structure and plate interface geometry shallower then 50 km depth come from wide-angle refraction studies conducted on and offshore the Nicoya Peninsula. Walther & Flueh (2002) imaged the Cocos Plate across the EPR–CNS plate suture in a trench-parallel direction. Their results indicated normal oceanic crustal structure and a low-velocity body near the plate suture, which was interpreted as an igneous intrusion at the base of the EPR-derived crust. Refraction line 300 imaged the trench-normal CNS side of the suture (Fig. 2) (Ye *et al.* 1996); along this transect the top of the Cocos Plate extends at a constant dip angle of 7° to ∼14 km depth, 90 km from the MAT. Across the EPR side of subduction, refraction line 101 extended from 20 km seaward of the MAT well landward of the volcanic arc (Fig. 2) (Christeson *et al.* 1999; Sallarès *et al.* 1999, 2001). Here the top of the subducted slab extends from 5 km depth at the MAT to 15–16 km depth at the coastline dipping shallowly at 6°, transitioning to 13° dip at ∼30 km from the trench (Christeson *et al.* 1999); by 40 km depth the plate dips ∼ 35° (Sallarès *et al.* 1999, 2001). These studies indicated that the Nicoya ophiolite complex comprising the peninsula extends offshore to form the margin wedge. *P*-wave velocities for this sequence range from ∼4.5–5.0 km s^{-1} depending on depth, with very low velocities (∼3.0 km s^{-1}) and high lateral velocity gradients within a small frontal prism composed of slope apron sediments and margin wedge material (Christeson *et al.* 1999). The Caribbean crust in northern Costa Rica is ∼40 km thick, nearly double the average Caribbean Plateau crustal thickness, and exhibits smoothly increasing velocities and densities with depth (Sallarès *et al.* 2001). Sallarès *et al.* (2001) proposed a formation sequence for the Costa Rica isthmus that includes magma generation, intrusion and underplating that thickened the Caribbean Plate and hydrated the forearc mantle.

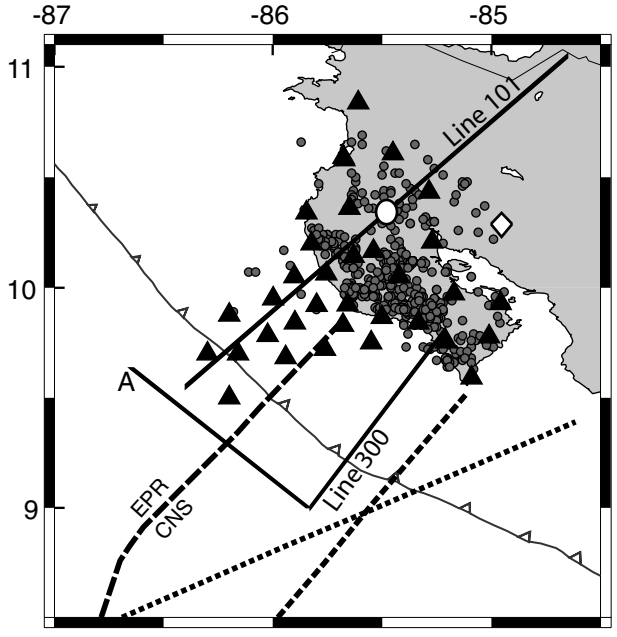

Figure 2. Nicoya Experiment 3-D inversion data set. 611 earthquakes within the network coverage were recorded by >10 *P*-wave arrivals (dark grey circles) and are subdivided from the minimum 1-D inversion data set for use in 3-D simultaneous inversion. Solid black lines mark seismic refraction and reflection information discussed in the text (Line 101:Christeson *et al.* 1999 and Sallarès *et al.* 1999, 2001; Line 300:Ye *et al.* 1996; A: Walther & Flueh 2002). Triangles: seismic stations; White circle: 1-D model reference station GUAI; diamond: GNS broad-band station JTS. Dashed lines: tectonic boundaries defined in Fig. 1.

3 METHODS

Local earthquake tomography (LET) techniques provide improved earthquake locations and seismic velocity information that in turn lends insight into the seismic and tectonic framework of a region. Calculation of traveltime to solve for earthquake location depends on earthquake phase picks, initial hypocentral location and velocity structure (e.g. Aki & Lee 1976; Crosson 1976; Ellsworth 1977; Kissling *et al.* 1984; Thurber 1981, 1992). In this study we use the LET algorithm SIMULPS13Q, an iterative damped least squares solution for local earthquake data that utilizes approximate ray tracing for computation of theoretical traveltimes (Thurber 1983; Eberhart-Phillips 1990; Evans *et al.* 1994). Using this technique, traveltime derivatives are extracted incrementally along small segments of the ray path, and velocities and hypocenters are iteratively updated to minimize arrival time misfit (e.g. Thurber 1983, 1993; Eberhart-Phillips 1986, 1990; Kissling *et al.* 1994). The complexity and resolution of the resulting velocity model depends on station spacing, earthquake distribution, subsurface structure and inversion parametrization, including choice of damping parameters and grid node spacing (Kissling *et al.* 2001).

We solve for the compressional wave velocity, V_P, and the ratio of the compressional and shear wave velocities, V_P/V_S, using the compressional wave arrival time, *P*, and the time difference between the shear and compressional waves, *S*–*P*, respectively. For real data sets, there is generally a significant decrease in quality and quantity of *S*-wave arrival identification, thus using *S*–*P* traveltimes to solve for V_P/V_S accounts for the inherent coupling between V_P and V_S across the same structure and minimizes induced artefacts due to differing resolution if V_P and V_S were calculated separately (e.g. Eberhart-Phillips 1990; Eberhart-Phillips & Reyners 1997; Reyners *et al.* 1999; Thurber & Eberhart-Phillips 1999; Wagner *et al.* 2005). Because compressional and shear waves are equally affected by density, changes in V_P/V_S can be directly related to Poisson's ratio, making it a useful tool for assessing petrologic properties.

Solutions of the linear approximation of the coupled hypocenter-velocity problem, such as the parametrization used by SIMULPS13Q, depend on choice of the initial reference model (Kissling *et al.* 1994). Poorly defined 1-D *a priori* models can introduce artefacts into the 3-D inversion that are not easily detected using standard resolution or covariance estimates (Kissling *et al.* 1994). Use of the 'minimum 1-D velocity model', or the optimal least squares solution of the coupled hypocenter-velocity model problem in 1-D for a given data distribution, decreases the possibility of artefacts induced by the initial reference model (e.g. Kissling *et al.* 1994). We use a minimum 1-D velocity model calculated using CRSEIZE Nicoya arrival time data within the 1-D inversion program VELEST (Kissling *et al.* 1995) as the initial starting model for 3-D LET (Table 1) (DeShon & Schwartz 2004). The Nicoya minimum 1-D model *P*-wave velocities agree well with the velocities modelled

using wide-angle refraction data at the same distance from the trench as the 1-D reference station GUAI (Sallarès *et al.* 1999, 2001). The initial V_P/V_S inversion begins at 1.78, which represents the average of the minimum 1-D V_P/V_S velocity model and is consistent with reported V_P/V_S studies in Costa Rica (Protti *et al.* 1995b; Quintero & Güendel 2000; DeShon *et al.* 2003). Station corrections from the 1-D inversion are not included as a starting parameter in the 3-D inversion because the 1-D inversion values reflect model uncertainties in calculating a flat-layered velocity model.

We relocate 611 earthquakes that occurred beneath the Nicoya CRSEIZE stations using the minimum 1-D velocity model prior to the full 3-D inversion (Fig. 2). These events have $\geq$10 *P*-wave arrivals and a greatest azimuthal *P*-wave separation of $\leq$180°. Recordings at Global Seismic Network (GSN) station JTS, a three-component broad-band station east of the Nicoya Gulf (Fig. 2), are included to expand the coverage of the array. Arrival quality is assigned to *P*- and *S*-wave data during initial processing (described further in DeShon 2004). Individual arrival quality factors range from 0–4, with 0 indicating highest quality picks (i.e. high signal-to-noise ratio, impulsive arrivals) and 4 being low-quality picks not appropriate for use in the inversion. Average *P*-wave picking error is estimated to be ~0.10 s and *S*-wave picking error is ~0.15–0.20 s.

In order to reduce artificial velocity smearing, earthquakes should be as evenly distributed as possible throughout the model such that rays cross from multiple directions and angles (e.g. Eberhart-Phillips 1990; Evans *et al.* 1994). The majority of local earthquakes used for inversion occur along the dipping plate interface and within the continental crust landward of the OBS and, therefore, data are not evenly distributed throughout the model space. Grid spacing is defined to minimize variability in the number of ray paths that sample each cuboid, or node-bounded parallelpiped. A coarse grid spacing of 20 × 20 km^2 places approximately one station per cuboid, and a finer grid spacing of 10 × 10 km^2 is applied beneath the peninsula where station spacing warrants (Fig. 3). Only grid nodes whose surrounding cuboids are sampled by $\geq$8 rays are included in the velocity inversion, and nodes outside of the station coverage remain fixed. Depth grid spacing is similar to the minimum 1-D model with minor revisions to regularize ray coverage (Table 1).

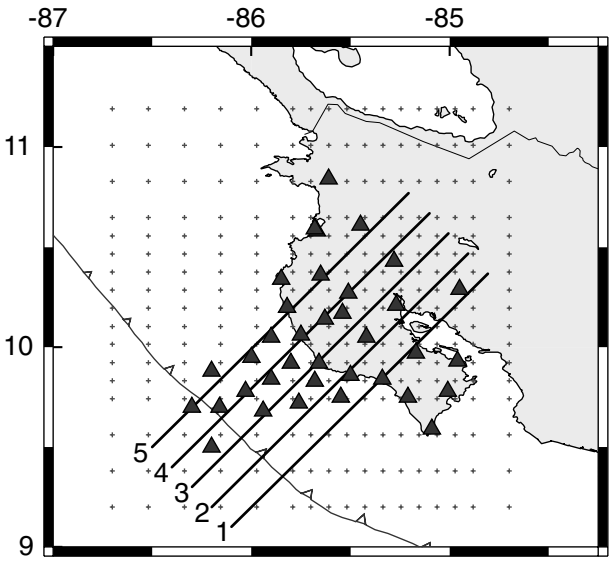

Figure 3. Coarse and fine grid spacing (crosses) used for progressive 3-D inversions. A 20-km-grid spacing was used to calculate the initial 3-D velocity structure and 10 km grid spacing was applied in regions of higher resolution. Solid black lines denote profiles through the model shown in later figures numbered sequentially from south to north. Triangles: seismic stations.

Table 1. Initial 1-D V_P and V_P/V_S velocity models used for 3-Dinversion (modified from DeShon & Schwartz 2004).

Depth (km)	V_P (km s^{-1})	V_S (km s^{-1})	V_P/V_S
−10.0	3.00	1.69	1.78
0.0	5.35	3.01	1.78
5.0	6.12	3.44	1.78
9.0	6.12	3.44	1.78
13.0	6.28	3.53	1.78
16.0	6.46	3.63	1.78
20.0	6.72	3.78	1.78
25.0	7.01	3.94	1.78
30.0	7.39	4.15	1.78
35.0	7.55	4.24	1.78
40.0	8.14	4.57	1.78
50.0	8.14	4.57	1.78
65.0	8.26	4.64	1.78
90.0	8.26	4.64	1.78
700.0	10.3	5.79	1.78

Progressive inversion schemes have been shown to yield smoother velocity changes and fewer artefacts then non-progressive schemes (e.g. Kissling *et al.* 1994; Eberhart-Phillips & Reyners 1999; Reyners *et al.* 1999; Husen *et al.* 2000, 2003a). Hence, we progressively iterate from 1-D, to a coarse 3-D, then a fine 3-D model such that results from the previous step are the initial conditions for the following step. First, we solve for a coarse grid V_P, then a coarse grid V_P and V_P/V_S, and finally a fine grid V_P and V_P/V_S. Extensive testing of alternative progression pathways indicated that the chosen path yielded a smoothly varying velocity model with fewer artefacts due to horizontal and vertically varying resolution, low variance, and geologically reasonable V_P and V_P/V_S (DeShon 2004).

Velocity and station parameter damping affect both the resulting velocity model and resolution estimates (Kissling *et al.* 2001), and properly choosing damping parameters ensures smoothly varying velocity models while minimizing data variance (Eberhart-Phillips 1986). We analyse trade-off curves for individual iterations with and without station corrections over a range of damping parameters (1–800) to find that value which minimizes data variance while maintaining low model variance (Eberhart-Phillips 1986). Choice of damping parameter also depends on *a priori* data quality (Kissling *et al.* 2001). Nicoya data picking errors are relatively low, so we choose the lowest damping value that minimizes data and model variance. For V_P, we choose a preferred damping of 50 for the coarse grid and 100 for the fine grid (Fig. 4a). Because the coarse grid 3-D V_P is the initial starting model for the V_P plus V_P/V_S inversion, the choice of damping for V_P/V_S proceeds with V_P held slightly overdamped (100). A preferred V_P/V_S damping of 50 is chosen (Fig. 4b). Station corrections account for traveltime residuals not incorporated into the 3-D velocity model and for near surface velocity characteristics not resolved due to data and network coverage (Eberhart-Phillips & Reyners 1999). Station corrections are damped in order to allow data residuals to be incorporated into the velocity model rather than the correction terms during the first inversion iteration. Calculation of station damping yields a preferred value of 10.

Earthquake locations are held fixed in the first iteration to guarantee data residuals are incorporated into the velocity model rather

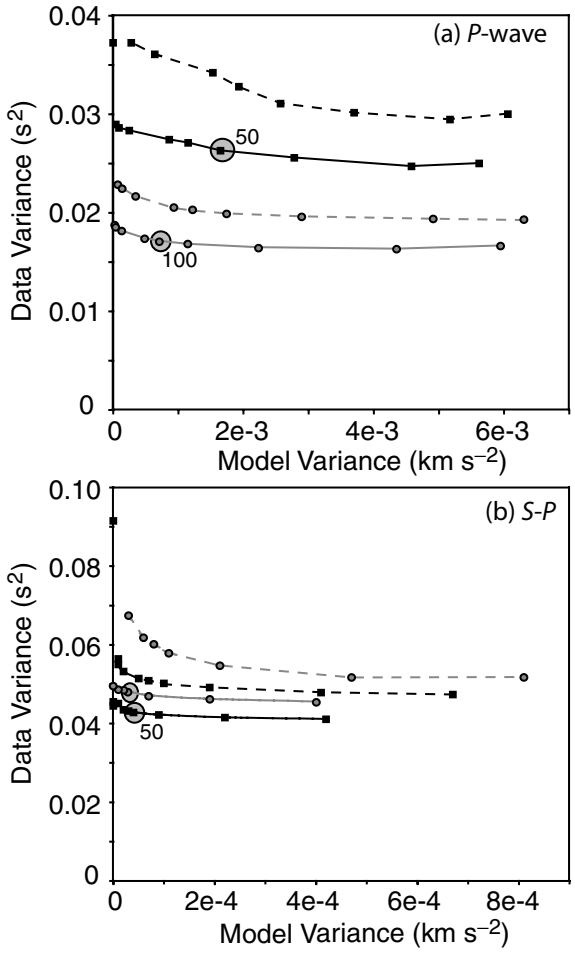

Figure 4. Trade-off curves of data versus model variance for coarse (black) and fine (grey) grid spacing. Curves are shown for single iteration inversions for both *P*(a) and *S*–*P*(b) arrival data with (solid) and without (dotted) station corrections. For the trade-off curves including station corrections, damping of 50 for *P* and *S*–*P* data with a station damping of 10 best minimize data and model variance. Fine grid and combined V_P and V_P/V_S inversions to explore damping begin from the appropriate preceding 3-D solution to maintain consistency with the progression used in this study. Testing damping parameters range from 5 to 800.

than systematic movement of earthquake locations or origin times (i.e. Husen *et al.* 2000, 2003a). When locations are not held fixed on the first iteration using the Nicoya data set, data misfit is expressed as large velocity perturbations in the shallowest layers and yields geologically unreasonable models (DeShon 2004).

4 RESOLUTION ESTIMATES

Model resolution is assessed using multiple methods (e.g. Eberhart-Phillips & Reyners 1999; Husen *et al.* 2000). To test amplitude and geometry recovery of the data set, we construct a synthetic arrival time data set using the hypocenters, arrival weighting and ray coverage of the data input into the 3-D inversion. We design a synthetic velocity model that reflects the broad scale geometry of the 3-D solution but assign opposite sign to expected anomalies to mathematically decouple the synthetic model from the real solution. This is called the characteristic velocity model (Haslinger *et al.* 1999). Computation of theoretical traveltimes through the characteristic model is preformed using the ART approach in SIMULPS13Q. We also examine resolution using derivative weighted sums (DWS: relative ray density in the vicinity of a model parameter) and the diagonal element of the full resolution matrix (RDE). The spread function, which is based on the relative values of the diagonal versus the rows of the full resolution matrix (Toomey & Foulger 1989; Michelini & McEvilly 1991), is calculated to better constrain velocity smearing at individual nodes.

The characteristic V_P model has a dipping −10 per cent anomaly that generally parallels the Cocos Plate, but with a steeper dip, and various crustal anomalies above the expected continental Moho. The mantle wedge region is assigned to be 10 per cent faster than the minimum 1-D model and is slightly offset landward in order to assess horizontal smearing between the slab and wedge region. All V_P anomalies are assigned to be ±10 per cent of the initial value at a grid point; V_P/V_S anomalies are either ±7.5 per cent or ±15 per cent of 1.78 (Fig. 5). Random noise is added to the synthetic traveltime data set prior to inversion such that arrivals with quality 0 are assigned noise between −0.02 and 0.02 s. This is linearly scaled so that arrivals with quality 3 are assigned noise between −0.18 and 0.18 s.

The synthetic arrival time data is used within the progressive inversion scheme to estimate smearing, expected velocity recovery and variable resolution. Due to the *a priori* data error, we cannot resolve velocity perturbations of less than ±1–2 per cent at a given depth. Fig. 5 consists of depth slices through the characteristic V_P and V_P/V_S models and the recovered velocity models. Note that V_P and V_P/V_S resolution, and specifically the location of velocity artefacts, varies significantly due to differences in data quality, data quantity and ray coverage. Fig. 6 consists of a cross-section along Profile 4 (Fig. 3) through a well-resolved region of the velocity model where the OBS extend seaward of the MAT. Due to the lack of OBS along the southern Nicoya Peninsula (Fig. 3, Profiles 1 and 2), V_P and V_P/V_S resolution varies significantly along MAT strike. There is little to no resolution of low-velocity layers above 5 km depth for both V_P and V_P/V_S (Fig. 5). Anomaly recovery offshore is also consistently poorer than beneath the land due to data distribution. The majority of earthquakes occur from 12 to 35 km depth, and at these depths V_P anomaly recovery averages 80–100 per cent of the prescribed anomaly beneath the peninsula and OBS array. In comparison, V_P/V_S anomaly recovery averages >80 per cent only along the northern and central regions of the peninsula. Below 40 km depth, recovery decreases to 50–80 per cent for both V_P and V_P/V_S, though the general pattern of the prescribed anomalies remains (Fig. 5). The dipping nature of the earthquake data set and a decrease in *S* waves recorded at the OBS introduce two significant artefacts attributed to ray path geometry:

(1) a high V_P artefact beneath the most landward OBS (Fig. 5, depth 0 and 9 km) and

(2) a high V_P/V_S artefact parallel to the subducting slab at 30–65 km depth (Fig. 6).

The dip, relative amplitudes and shape of features introduced in the characteristic model are well recovered, though some smearing is evident in both the V_P and V_P/V_S models (Fig. 6). As noted in plane view, V_P/V_S resolution is significantly poorer than V_P resolution. Anomaly recovery decreases 170–220 km from the trench axis, and hence the high V_P, low V_P/V_S velocity anomaly placed at 40–65 km depth to represent the expected location of the forearc mantle wedge could be resolved only at the tip of the continental Moho/oceanic slab intersection. Amplitude recovery of the seaward tip of this anomaly only reaches ∼65 per cent of the initial 10 per cent and −15 per cent prescribed V_P and V_P/V_S, respectively (Fig. 6). At these depths,

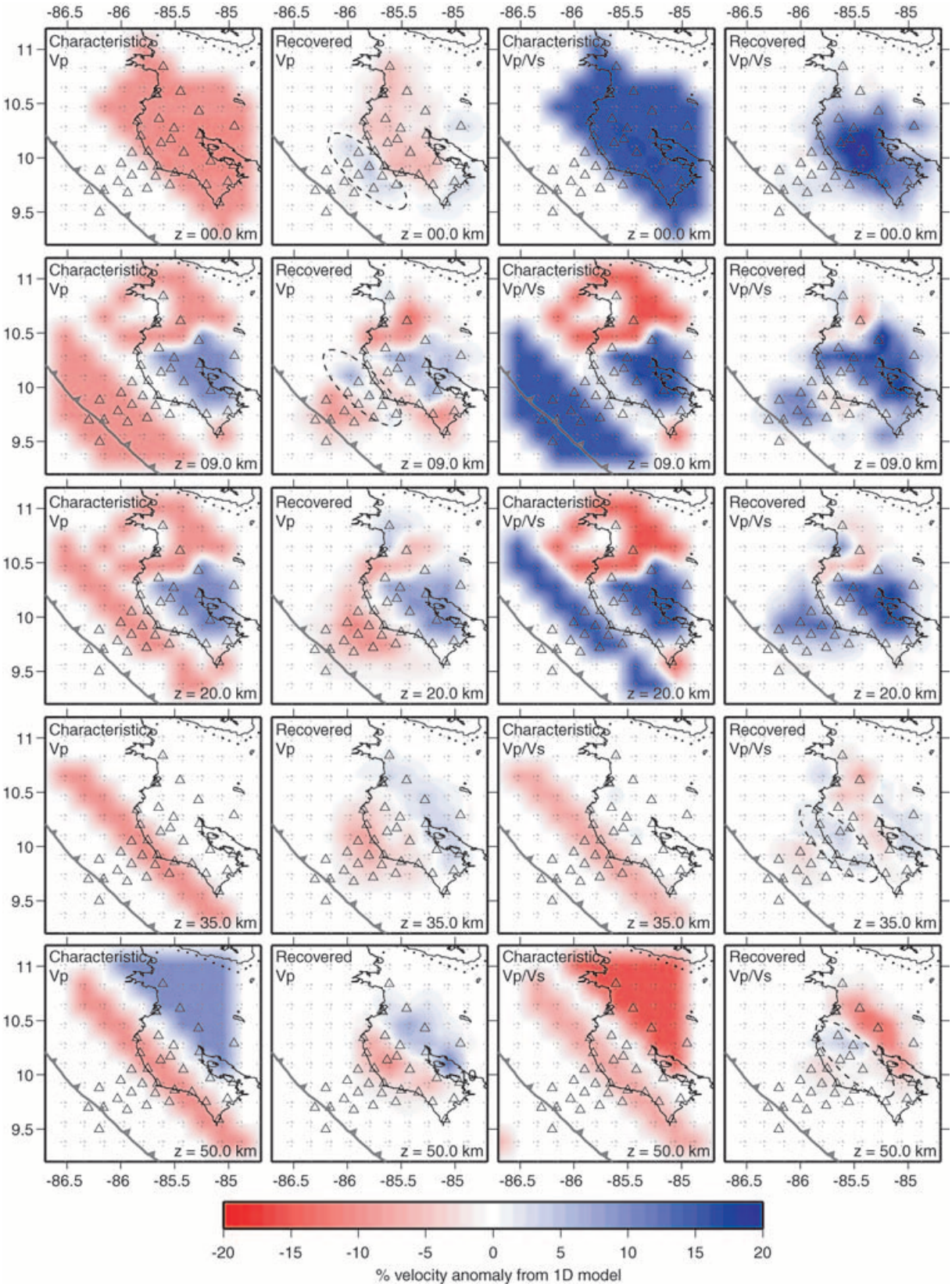

Figure 5. Depth planes through the characteristic velocity model (columns 1 and 3) and restoring resolution V_P (column 2) and V_P/V_S (column 4) results using synthetic arrivals times with noise. Colours represent velocity anomaly from the initial 1-D velocity model. Stations are shown as open triangles. Features discussed in text marked with dashed lines.

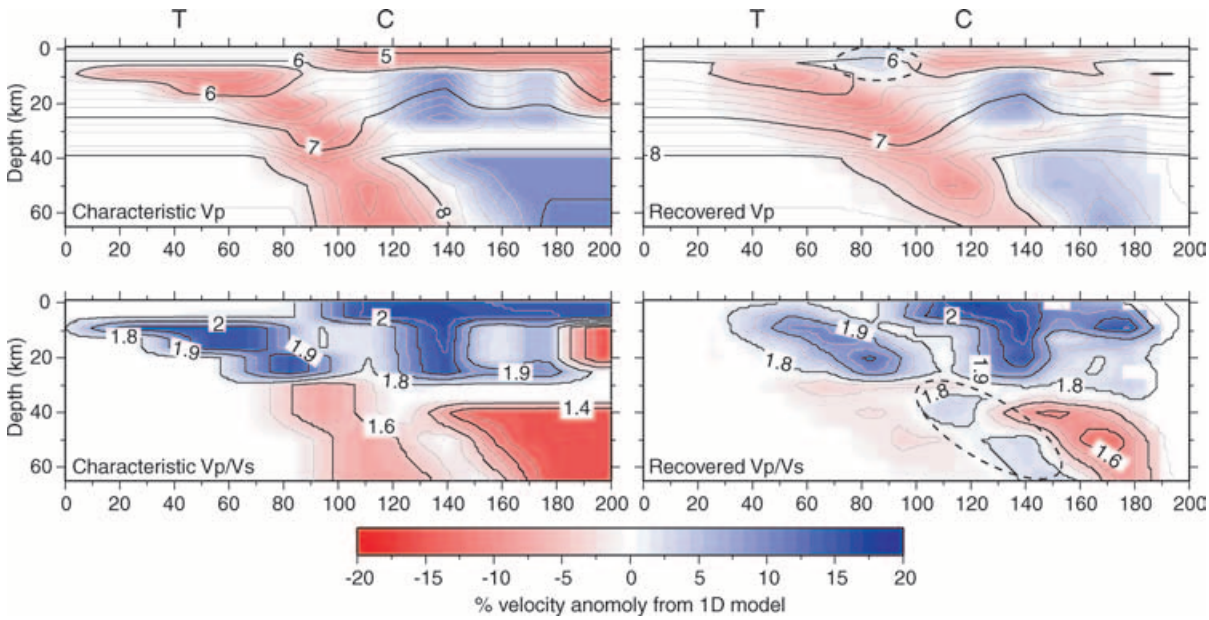

Figure 6. Representative cross-section along Profile 4 (shown in Fig. 3) through the characteristic V_P and V_P/V_S velocity models (column 1), and the recovered V_P and V_P/V_S models (column 2). Colours represent velocity anomaly from the initial 1-D velocity model; contours represent absolute V_P or V_P/V_S. T and C represent the MAT and coastline locations, respectively. Features discussed in text marked with dashed lines.

this anomaly recovery corresponds to a V_P amplitude difference of $\sim$0.5 km s^{-1} and a V_P/V_S difference of $\sim$0.2 compared to the absolute V_P and V_P/V_S in the characteristic velocity model. The synthetic V_P/V_S model clearly fails to recover the abrupt change in V_P/V_S along the dipping slab feature at 30 km depth (Fig. 6), limiting interpretation of the oceanic crust/mantle V_P/V_S.

Calculation of the full resolution matrix for the last iteration of each progressively finer inversion yields important information on spatial resolution. DWS and RDE largely track over the model space while spread function varies over the Nicoya Peninsula study area. Based on the results from the characteristic V_P and V_P/V_S models (Figs 5 and 6), we use regions with spread function $\leq$2.5, RDE $>$0.04, and DWS $\geq$50 to define the resolution boundaries of the velocity model for interpretation purposes (Figs 7 and 8). Due to the hypocenter and station geometry, velocities beneath the peninsula and above the subducting slab are much better resolved than at the edges of the model.

5 RESULTS

The final fine grid results utilize 7598 *P*- and 5761 *S*-wave arrivals (Fig. 3), and results have a combined rms of 0.14 s and data variances of 0.010 s^2 for *P* and 0.035 s^2 for *S*–*P*. The initial rms of the data set prior to 1-D inversion calculated on a subset of 475 events was 0.43 s, and data variances were $\sim$0.29 s^2 for *P* and 0.32 s for *S*–*P* (DeShon 2004). Prior to 3-D inversion *P* and *S*–*P* data variances were 0.04 s^2 and 0.11 s^2, respectively, with a total rms of 0.16 s. Note the largest drop in variance occurs during 1-D inversion for hypocenter parameters, velocity model and station corrections.

The mean absolute value changes in event locations following 3-D inversion are 0.54, 0.67 and 1.64 km (north, east, depth) relative to the 1-D inversion locations. Changes relative to initial catalogue locations calculated using the IASP91 velocity model are 0.35 s origin time and 0.84, 1.01 and 2.86 km (north, east, depth). The algorithm provides formal 1σ hypocenter uncertainties, which do not account for systematic biases and may significantly underestimate true errors (e.g. *Husen et al*. 2003b). The 2σ hypocenter uncertainty estimates are 0.10 s origin time and 0.58, 0.60 and 1.04 km (north, east, depth). The 2σ uncertainty spans the mean location shift moving from the 1-D to 3-D inversion solution fairly well.

The correlation between earthquake activity and seismic velocity structure varies with depth. Fig. 7 shows depth slices through the final 3-D model in absolute V_P and V_P/V_S and in relative V_P and V_P/V_S anomalies compared to the 1-D initial model. Fig. 8 shows V_P and V_P/V_S cross-sections in absolute and relative anomaly perpendicular to the MAT (shown in Fig. 3) and includes earthquakes located within 7.75 km of the cross-section plane. Regions with DWS $<$50 and spread function $>$2.5 are masked in grey to indicate areas of poorer resolution. For clarity, results are discussed by feature.

5.1 Station corrections and surface geology

Structure above 5 km depth is not adequately sampled by this data set. The peninsula largely appears faster than the 1-D model prediction, possibly due to the high-velocity ophiolites composing the Nicoya Complex underlying the peninsula. The small and spatially dispersed *P*-wave station corrections for land seismometers indicate little variance in near surface velocities (Table 2). *S*-wave corrections for the land stations reflect the presence of surface sediments. Corrections are skewed towards high, positive values suggesting V_P/V_S is too high beneath the stations, an artefact noted with synthetic data. High, positive *P*-wave corrections at OBS located along the forearc are likely due to model sensitivity in this region (Figs 5 and 6). V_P/V_S station corrections for the OBS are relatively low, which reflect the small number of *S*–*P* traveltimes picked (generally $<$20 *S*-wave arrivals/station) on the noisier OBS.

5.2 Plate interface seismicity and velocities

Previous *P*-wave refraction studies along Line 101 (Fig. 2) presented plate interface interpretations for the central Nicoya Peninsula (Christeson *et al.* 1999; Sallarès *et al.* 1999, 2001). Along

Table 2. Station locations with V_P and V_S station corrections for the Nicoya Peninsula experiment.

Station	Lat (°)	Lon (°)	*P* Correction (s)*	*S* Correction (s)*
BANE	9.93	−84.96	−0.05	0.33
BONG	9.75	−85.21	−0.13	0.45
COND	10.58	−85.67	−0.03	0.20
CORO	9.97	−85.17	−0.08	0.31
COYO	10.36	−85.65	0.02	0.36
GRAN	10.34	−85.85	0.10	0.19
GUAI	10.27	−85.51	0.02	0.38
GUIO	9.92	−85.66	−0.18	0.47
HATA	10.43	−85.28	0.15	0.25
HOJA	10.05	−85.42	−0.07	0.32
INDI	9.86	−85.50	−0.11	0.42
JTS	10.29	−84.95	−0.22	−0.15
JUDI	10.17	−85.54	−0.01	0.28
MARB	10.06	−85.75	−0.09	0.37
NB01	9.50	−86.20	0.00	0.00
NB03	9.70	−86.16	−0.14	1.07
NB04	9.70	−86.30	0.00	0.00
NB05	9.88	−86.20	−0.01	−0.07
NB06	9.78	−86.03	−0.05	−0.14
NB07	9.68	−85.94	−0.01	0.07
NB08	9.72	−85.76	0.39	0.51
NB09	9.84	−85.90	0.40	0.00
NB10	9.95	−86.00	0.35	−0.21
NB11	10.05	−85.90	0.45	0.15
NB12	9.92	−85.80	0.46	0.00
NB13	9.83	−85.68	0.38	0.02
NB14	9.75	−85.55	0.27	0.00
PAPA	10.59	−85.68	0.01	0.17
PARG	10.20	−85.82	−0.09	0.36
PNCB	9.59	−85.09	0.01	0.42
PNUE	9.84	−85.34	−0.16	0.41
SAJE	10.61	−85.45	0.11	0.28
SARO	10.84	−85.61	0.15	0.11
TFER	10.21	−85.27	−0.06	0.34
VAIN	9.78	−85.01	−0.07	0.33
VIMA	10.14	−85.63	−0.08	0.19

Profile 4 (Fig. 3), which broadly parallels Line 101, the plate interface is set to the refraction interpretations. The Nicoya Peninsula minimum 1-D model used as the initial condition for velocity inversion closely mimics expected velocities for the top of the oceanic plate. Thus we expect the 0 per cent V_P anomaly contour to represent the top of the subducting slab (Figs 7 and 8). Comparison between the refraction data and the −5 per cent to 0 per cent V_P anomaly contour is very good along Profile 4, and hence the −5 per cent to 0 per cent anomaly contour is used to guide the choice of the top of the subducting plate interface to about 40 km depth on other profiles. Resolution beneath the OBS array limits identification of the plate interface at <9 km depth, but intuitively the plate interface should move progressively deeper inland starting from the seafloor depth at the trench (∼4 km; Fig. 7a). Below 40 km depth the plate interface interpretation is based on the location of the interface from refraction data and on the extension of plate curvature. We use a continuous curvature interpolation technique to contour the surface of the plate interface between cross-sections (Smith & Wessel 1990) and project them onto the velocity images to facilitate interpretation (Figs 7 and 8).

We distinguish between interplate and intraplate seismicity across the Nicoya Peninsula by interpreting those earthquakes occurring directly on or above the plate interface (−5 to +8 km) between 0–40 km depths as interplate seismogenic zone events. This method helps to account for errors in plate interface interpretation. Calculation of focal mechanisms is ongoing, but the majority of events interpreted as interplate in this study are consistent with underthrusting along the plate interface (Hansen *et al.*, 'Relocations and focal mechanisms determined from waveform cross-correlation of seismic data from the Nicoya Peninsula, Costa Rica', submitted to Bull. Seis. Soc. Am.). We define the up- and downdip limits of interplate microseismicity using the range of interplate seismicity (Fig. 9). The Nicoya earthquakes have low errors ($\leq$1 km at 2σ), and the Gaussian distribution approach outlined by Pacheco *et al.* (1993) commonly utilized to define the updip and downdip limits of seismicity (e.g. Husen *et al.* 1999; DeShon *et al.* 2003) may underestimate the extent of the plate interface hosting small magnitude earthquakes. Consideration of data range places the updip limit for CNS and EPR sides of the plate at 12 and 17 km depth, respectively, and the downdip limits at 26 and 28 km depth, respectively. A robust offset in depth at onset of microseismicity (∼5 km) remains at the transition between CNS and EPR crust (Fig. 9). This depth offset was first noted by Newman *et al.* (2002), who estimated an ∼10 km offset, with EPR microseismicity beginning at 20 km depth BSL and CNS microseismicity at 10 km depth BSL. The mean absolute location differences between this study and Newman *et al.* (2002) are 0.76, 0.99 and 2.28 km (north, east, depth). Along the subducted plate suture, microseismicity extends nearly 5 km closer to the MAT in map view, locally extending the updip extent of microseismicity to ∼10 km depth (Fig. 9).

We examine five cross-sections along the peninsula to investigate small-scale variability in earthquake locations and velocities and to identify inter- and intraplate events. One source of error in this approach results from the arbitrary cut-off used to distinguish between shallow interplate and intraslab seismicity beneath 40 km depth. Intraslab earthquakes may be misidentified as interplate, and vice versa.

An ∼11 km southwestward step in the plate interface is apparent near the projected downdip EPR/CNS plate suture, indicating that the subducting CNS-origin crust dips more shallowly than does the EPR-generated crust in the north (Figs 7a and b). Steepening of the plate interface from south to north has been observed in previous refraction and Wadati-Benioff zone studies along Costa Rica (e.g. Protti *et al.* 1994, 1995a; Ye *et al.* 1996). Below ∼20 km depth this offset is not apparent (Fig. 7c).

Interplate seismicity generally forms a dipping planar feature, but in the southern Nicoya Peninsula microseismicity occurs in a more diffuse region around the plate interface (Fig. 8a, Profiles 1 and 2). Microseismicity along the south of the peninsula begins between 7.5 and 11.5 km depth but well landward of the plate interface (Figs 7a and 8a, Profiles 1 and 2). By 13–14.5 km depth in the southern and by 14.5 and 17.5 km in the northern Nicoya Peninsula microseismicity occurs along the plate interface (Fig. 8). Activity along the EPR/CNS suture, approximately located along Profile 3 (Fig. 3), notably decreases by 17.5–22.5 km depth (Fig. 8a). A decrease in the spatial density of microseismicity across the CNS/EPR boundary, with fewer events occurring on the EPR side, does not appear to be due to a bias in earthquake selection since station coverage is denser along the northern Nicoya Peninsula.

Interplate activity is associated with a negative V_P anomaly that parallels the plate interface to a depth of ∼20 km, with absolute velocities of 5.2–5.8 km s^{-1} (Fig. 8a). Along the EPR interface the updip limit of interplate microseismicity abruptly occurs where the negative V_P anomalies terminate (Fig. 8a, Profiles 3–5). Along the northern Nicoya Peninsula, a small, negative V_P/V_S anomaly

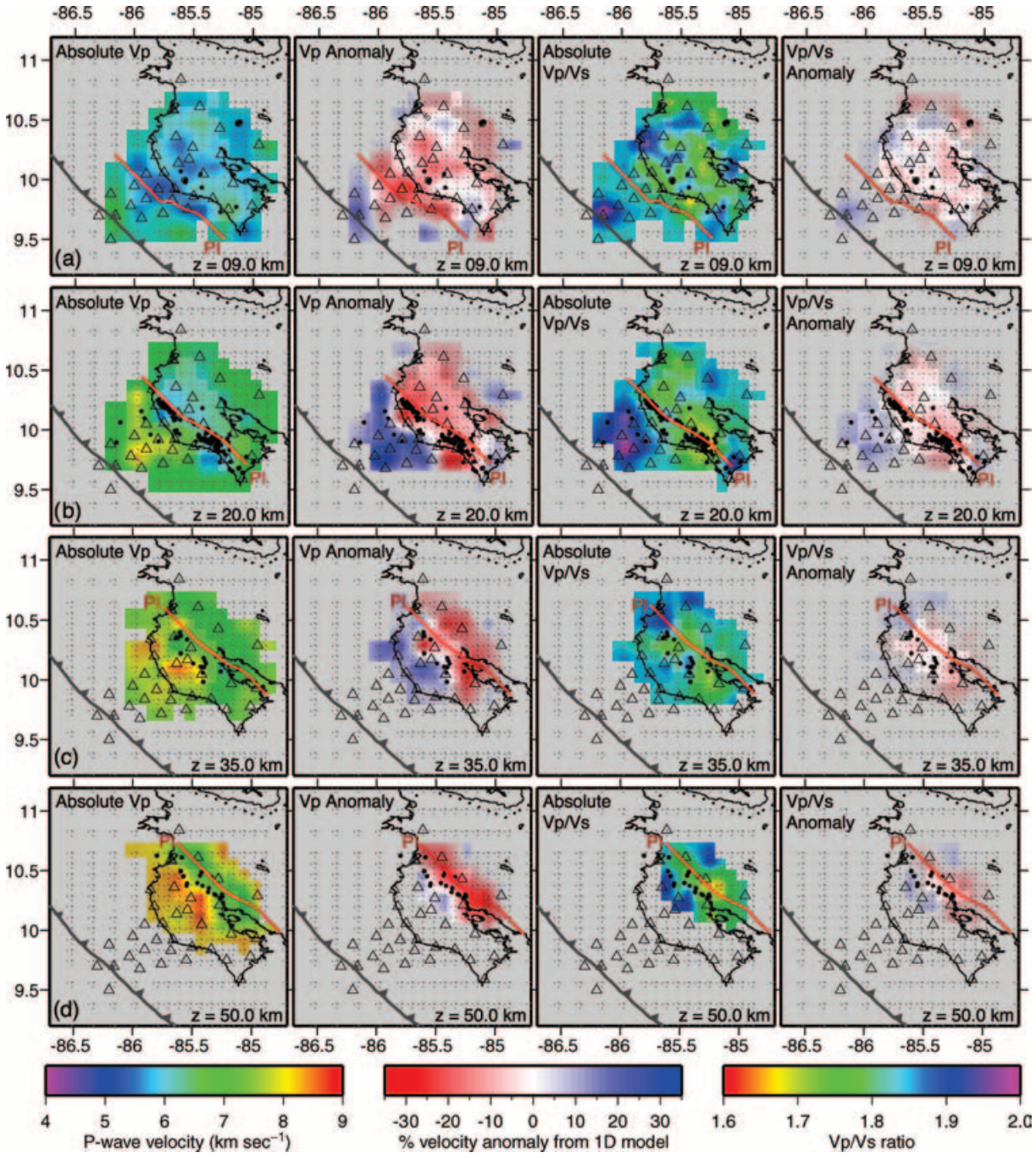

Figure 7. Depth planes through absolute and relative V_P (column 1 and 2) and absolute and relative V_P/V_S (column 3 and 4). Earthquakes (solid circles) are projected to nearest plane, and the plate interface contours at each depth (red line; PI) are interpreted as described in the text.

coincides with reduced V_P (Fig. 8a). These absolute velocities are broadly consistent with predicted values for margin wedge of Nicoya Complex composition (Sallarès *et al.* 1999, 2001) and oceanic upper crust velocities (i.e. Walther & Flueh 2002). Langseth & Silver (1996) and Ranero *et al.* (2003) proposed that normal faulting within the Cocos Plate along the outer rise introduces water into the oceanic crust, which could account for the noted V_P reduction. Alternately, the EPR oceanic crust may be hydrated prior to reaching the outer rise normal faults due to hydrothermal circulation (Hutnak *et al.* 2006).

5.3 Continental Moho location and mantle wedge velocities

Previous studies placed the continental Moho between 32 and 38 km depth beneath the Nicoya Peninsula and suggested that the velocity contrast across the crust/mantle boundary is very small (Matumoto *et al.* 1977; Protti *et al.* 1996; Quintero & Kulhanek 1998; Sallarès *et al.* 2000, 2001; Husen *et al.* 2003a; DeShon & Schwartz 2004). Inspection of profiles through the V_P model indicate a turnover in the 7.0–7.2 km s^{-1} V_P contours between 30 and 40 km (Fig. 8) that

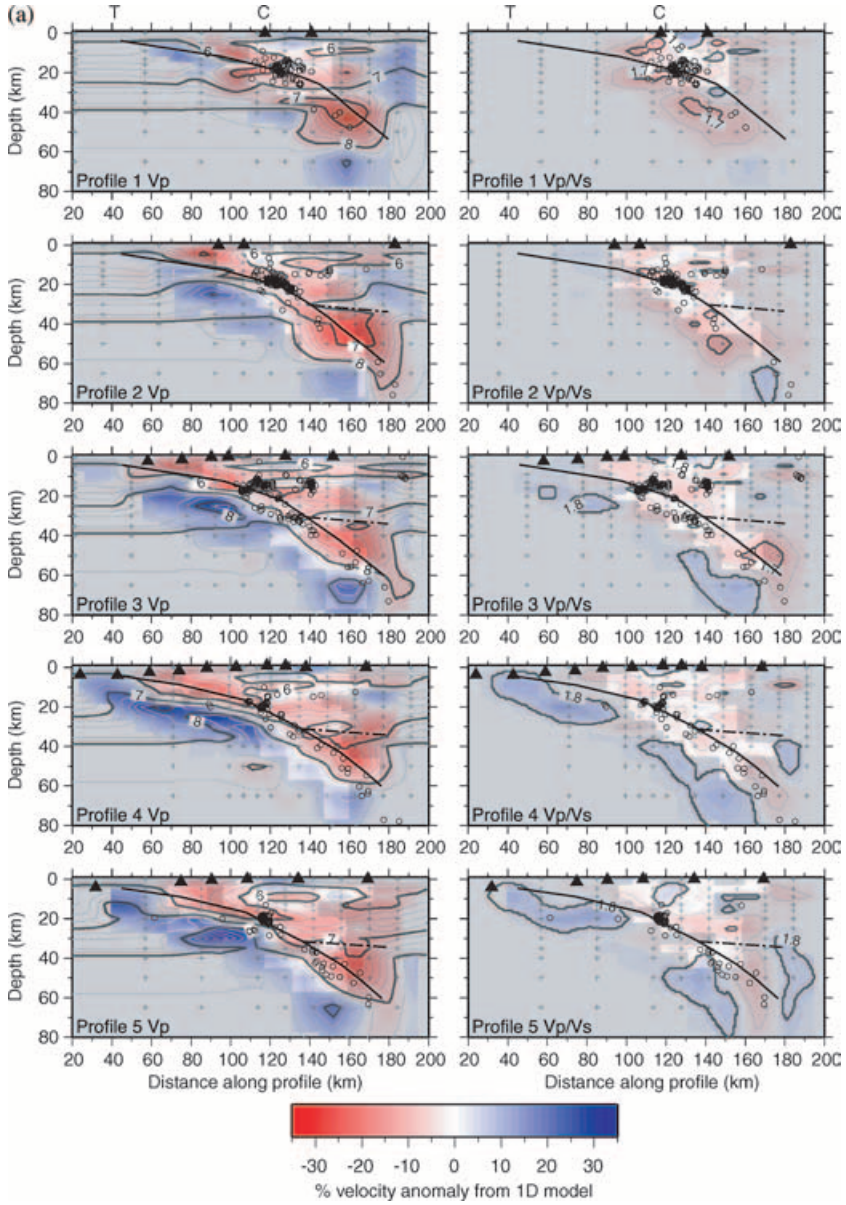

Figure 8. (a) Cross-sections through relative V_P (column 1) and V_P/V_S (column 2). Earthquakes (open circles) and stations (inverted triangles) are projected to the nearest cross-section. Plate interface (black line) and continental Moho (dash-dot black line) interpretations are described in the text. Contours represent absolute V_P and V_P/V_S. Regions of lower resolution are shaded grey. (b) Resolution of profiles through the V_P and V_P/V_S models. Shown is derivative weighted sum (DWS). The thick black lines mark regions where DWS < 50, RDE > 0.04, and spread function ≤ 2.5. Profile locations from Fig. 3.

we infer to represent the continental Moho. Such *P*-wave velocities are consistent with lower continental crust based on refraction data (Sallarès *et al.* 1999, 2001). However, we recognize that the error associated with this interpretation cannot be constrained due to the expectedly small velocity contrast. To the south, the continental Moho intersects the downgoing slab at ∼30 km depth (Profile 2, Fig. 8a). The mantle forearc wedge exhibits slow *P*-wave velocities, averaging 6.8–7.0 km s^{-1} (Fig. 8a), and the downdip limit of seismogenic zone seismicity is ∼5 km updip of the intersection of the continental Moho and the subducting slab. Along the northern Nicoya Peninsula, the continental Moho intersects the slab at 30 km depth with mantle wedge V_P at 7.0–7.2 km s^{-1} (Profiles 3–5, Fig. 8a). V_P/V_S in the mantle wedge along EPR profiles ranges between 1.73 and 1.78, and interplate seismicity occurs ∼10 km updip of the Moho/slab intersection (Fig. 8). Overall, along the Nicoya Peninsula the continental Moho intersects the downgoing slab between 30 and 34 km depth.

5.4 Caribbean crust seismicity and velocity

Refraction studies constrained continental crust V_P to be 4.5–7.0 km s^{-1}, increasing with depth (Christeson *et al.* 1999; Sallarès *et al.* 1999, 2001). Sallarès *et al.* (1999, 2001) divided the continental crust into upper, mid and lower levels with corresponding *P*-wave velocities of 5.3–5.7 km s^{-1} (0–10 km BSL), 6.2–6.5 km s^{-1} (5–20 km BSL) and 6.9–7.3 km s^{-1} (20–40 km BSL). Fig. 10 superimposes the crustal structure from Sallarès *et al.* (1999, 2001) on a generalized interpretation of subduction zone structure along Profile 4 (see Fig. 3 for profile location). The V_P of the two models of continental crustal structure generally agree, with the largest V_P

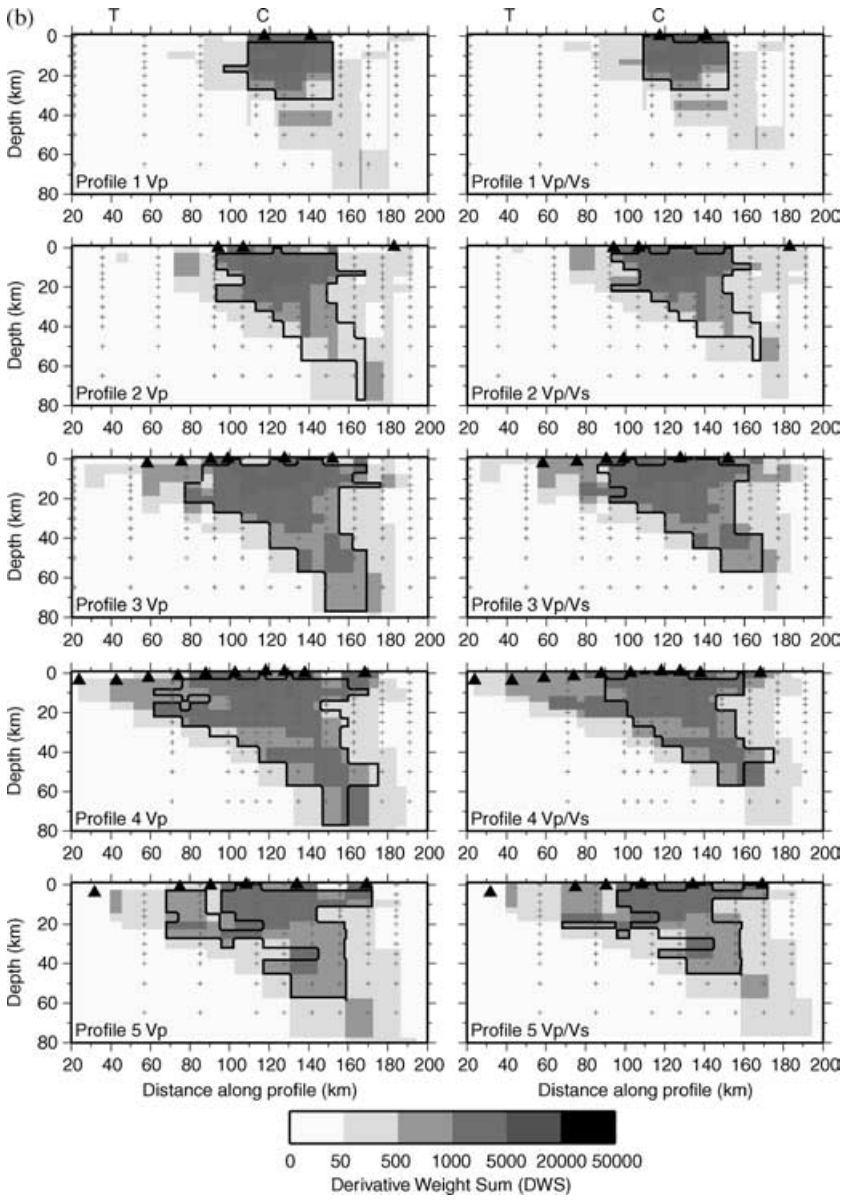

Figure 8. (*Continued.*)

discrepancy occurring beneath the coastline between 0 and 15 km depth.

Decreasing velocity model resolution and the lack of refraction data beneath the southern Nicoya Peninsula complicates interpretation of crustal versus interplate seismicity. Along Profile 1, seismicity forms a dipping plane generally paralleling the plate interface but outside the bounds used in this study (Fig. 8a). These earthquakes occur within the upper plate, but the events are likely related to local subduction processes.

5.5 Oceanic plate velocities and intraslab earthquakes

Earthquakes occurring within the oceanic crust form a sparsely populated dipping feature that extends from 18 to >80 km depth (Fig. 9). We primarily interpret the oceanic Moho by maintaining a crustal thickness of 7 km, consistent with refraction information (Fig. 10) (Ye *et al.* 1996; Christeson *et al.* 1999; Sallarès *et al.* 1999, 2001; Walther & Flueh 2002). In the northern Nicoya Peninsula, the oceanic mantle appears relatively fast in V_P, ranging between 8.1 and 8.4 km s^{-1}. Variations in V_P within the oceanic crust and mantle beneath the southern Nicoya Peninsula are likely due to low ray coverage (i.e. poor solution quality). Because of the limited timing and distribution of the OBS and seismicity, an insufficient number of long ray paths penetrated the mantle beneath the oceanic crust for analysis.

6 DISCUSSION

Possible mechanisms controlling the transition from aseismic to seismic behaviour along the updip limit of seismogenic zones include the mechanical backstop model (Byrne *et al.* 1988), temperature-controlled mineral transition models (Vrolijk 1990; Hyndman *et al.* 1997), and combinations of pressure- and temperature-dependent material characteristics such as variable pore fluid pressure and cementation (Moore & Saffer 2001; Saffer & Marone 2003; Moore *et al.* 2006). Comparisons of thermal modelling to seismogenic zone seismicity rupture limits across many

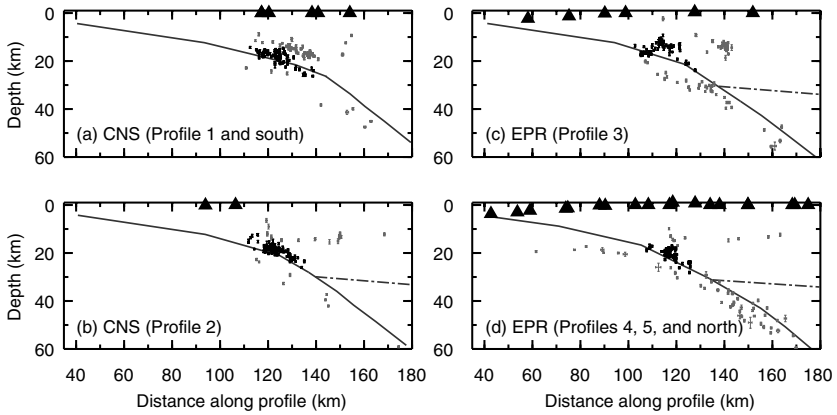

Figure 9. Cross-sections moving south to north through hypocenters resulting from 3-D inversion. Earthquakes are shown with error bars and divided into earthquakes identified as seismogenic zone interplate seismicity (black) and intraplate seismicity (grey). Stations are projected onto the nearest profiles (triangles). The preferred plate interface interpretation from each cross-section is shown for reference (dark grey line). Note the increasing dip angle of subduction from south to north (from a to d). Profile locations are shown in Fig. 3. All seismicity and stations occurring south of Profile 1 and north of Profile 5 are included in cross-sections a and d, respectively.

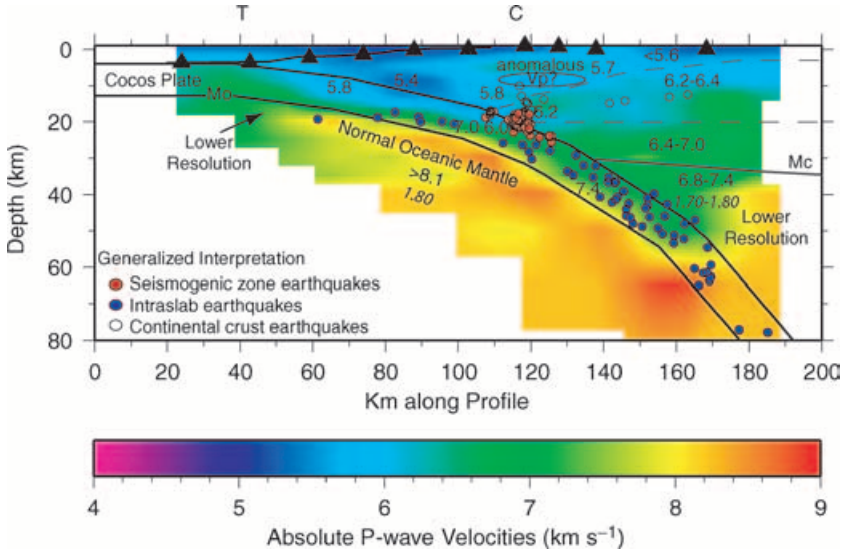

Figure 10. Generalized interpretation of the Nicoya Peninsula 3-D velocity models and associated hypocenters. Colour and values indicate V_P ; V_P/V_S shown in italics. The observed velocities agree well with *P*-wave velocities and crustal structure (dashed black lines) from wide-angle refraction data (Sallarès *et al.* 2001). The updip limit of interplate seismicity (red circles) may correspond to the mid crust/oceanic slab interface, identified by the transition from 5.8 to 6.4 km s^{-1} *P*-wave velocities. The continental Moho (Mc) appears between 32 and 40 km depth BSL, and the downdip limit of microseismicity clearly occurs updip of the continental Moho/oceanic slab intersection. The forearc mantle wedge may be 15–30 per cent hydrated based on decreased *P*-wave velocities and slightly elevated V_P/V_S. The oceanic Moho (Mo) is well resolved, and oceanic mantle *P*-wave velocities are normal with slightly elevated V_P/V_S.

subduction zones have shown that seismicity generally occurs between the ∼100–150°C and 350°C isotherms (Hyndman & Wang 1993; Hyndman *et al.* 1997; Oleskevich *et al.* 1999; Currie *et al.* 2002; Harris & Wang 2002). For low-temperature subduction zones and oceanic subduction zones, Hyndman *et al.* (1997) suggested the downdip transition occurs when the downgoing plate encounters the upper forearc mantle before temperatures reach 350°C, the onset of ductility in common subduction component materials. Dehydration of subducted sediments and oceanic crust at these depths can introduce water into the continental mantle. Serpentinite, a hydrated peridotite-related mineral assemblage possibly created by this water, has been shown to be conditionally stable in a frictional sense, exhibiting seismic behaviour under increasing applied stress or higher rupture velocities (e.g. Hyndman & Peacock 2003).

Previous studies utilizing the CRSEIZE earthquake data set suggested that the updip limit of microseismicity across the Nicoya Peninsula broadly corresponded to the 100–150°C isotherm estimate along the plate interface (Harris & Wang 2002; Newman *et al.* 2002). Spinelli & Saffer (2004) performed a 3-D thermal model for the region and concluded that the onset of seismicity likely represented the transition to stick-slip behaviour due to fluid pressure dissipation and increased effective normal stress. Both the Harris & Wang (2002) and Spinelli & Saffer (2004) thermal models incorporated cooling due to 0–2 km of hydrothermal circulation on the EPR-derived crust and varied shear heating along the subduction thrust to assess the downdip thermal affects of EPR and CNS lithosphere. Because geodetically derived interface locking models and prior large earthquakes show that the shallow subduction zone updip

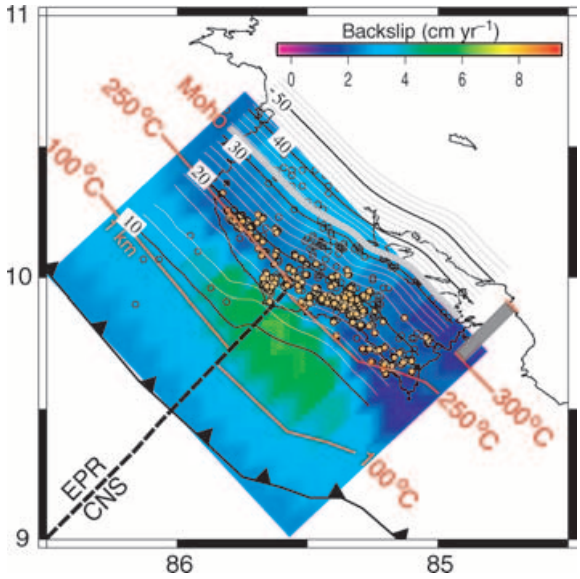

Figure 11. Geodetically inferred locking and interplate seismicity (orange circles) along the plate interface. Interplate seismicity occurs downdip of a major zone of locking which corresponds to nearly 75 per cent of the plate rate in this region. Microseismicity concentrates where the plate creeps. Geodetic model from Norabuena *et al.* (2004). Temperature isotherms from Spinelli & Saffer (2004) updip and Harris & Wang (2002) downdip; the grey box indicates the potential variance in the modelled 300°C isotherm. Thick grey line marked 'Moho' represents the intersection of the subducting plate with the continental Moho estimated in this study.

of ∼20 km depth is susceptible to failure in large earthquakes, the CRSEIZE microseismicity does not constrain the upward extent of potential subduction megathrust earthquakes in this region (Fig. 11) (Norabuena *et al.* 2004).

Schwartz & DeShon (2006) compared the earthquake relocations presented in this study with geodetic locking models (Norabuena *et al.* 2004) and thermal models (Harris & Wang 2002; Spinelli & Saffer 2004). They concluded that plate interface microseismicity more closely correlates to the 250°C isotherm estimate, a temperature at which most mineral transitions in oceanic sediments have already taken place (Fig. 11), while the onset of shallow plate locking corresponds well with the modelled 100°C isotherm (Fig. 11). Based on this observation, Schwartz & DeShon (2006) suggested that two transitions in mechanical behaviour occur along the plate interface:

(1) the transition to stick-slip behaviour as marked by increased locking across the plate interface and

(2) the transition to a geodetically creeping zone that is capable of producing microseismicity. The transition to creep and microseismicity may result from increased pore fluid pressure across the plate interface resulting from basalt dehydration reactions in a hydrated oceanic plate and/or decreased permeability in the upper plate that both begin at ∼250°C. Small decreases in effective normal stress may lead to fault weakening and generation of microseismicity downdip of the more strongly coupled, geodetically locked region. This hypothesis explains why the onset of microseismicity reflects the thermal state of the incoming plate but corresponds to higher temperatures.

Alternately, the onset of microseismicity between 12 and 17 km depth may mark a small modification in frictional stability across the plate interface due to a change in composition of the upper plate. Continental crustal structure interpretations for the Nicoya Peninsula region based on *P*-wave refraction data suggested Nicoya Complex flood basalts transition to a basalt–gabbro composition at these depths (Sallarès *et al.* 2001). Nicoya Complex materials are expected to have a lower V_P than mid-crust level basalt–gabbro rocks along the plate interface (Sallarès *et al.* 2001), similar to imaged V_P at the onset of interplate seismicity (5.8–6.4 km s^{-1}; Fig. 10). This model does not explain the along-strike depth transition at the CNS–EPR plate suture nor the temperature correlation. However, steepening of the slab across the suture could lead to a vertical offset of the mid-crust/oceanic slab intersection seen in microseismicity.

The degree of subduction erosion beneath the Nicoya forearc could vary spatially along-strike and explain local variations in seismicity along the peninsula. Subduction erosion may be indirectly related to temperature if hydrofracturing of the upper plate plays a key role in the erosional process, as proposed by Ranero & von Huene (2000) and von Huene *et al.* (2004). Additionally erosion could introduce a large amount of upper plate material into the subduction channel (von Huene *et al.* 2004). The amount and depth range of sediment, fault gouge, and basalt dewatering and consolidation is affected by temperature. The above described processes could decrease pore fluid pressure and increase effective normal stress or change the mechanical strength of the plate contact zone with depth, perhaps explaining the variable onset of locking and seismicity along the plate interface.

The downdip limit of interplate microseismicity along the Nicoya Peninsula occurs at 26–28 km depth BSL. The continental Moho intersects the downgoing slab in this region between 30 and 35 km depth, 95 and 105 km from the MAT, downdip of seismogenic zone microseismicity (Fig. 10). Thermal modelling studies allowing small amounts of shear heating have placed the 300–350°C isotherm, the expected temperature controlling the onset to ductile behaviour, less than 100 km from the trench (Harris & Wang 2002; Peacock *et al.* 2005). One caveat, however, is that, like the updip limit, inspection of aftershock regions of $M_w > 6.9$ earthquakes indicate that the potential seismogenic zone extends beyond the downdip extent of the interplate microseismicity we recorded in the interseismic period (compare Figs 1 and 11). Error bars associated with the 300–350°C isotherm overlap with the continental Moho/oceanic slab intersection, precluding a unique interpretation of processes involved in controlling the downdip extent of microseismicity (Fig. 11).

DeShon & Schwartz (2004) reported multiple lines of evidence, including receiver function modelling at GSN station JTS, for the presence of serpentinized mantle wedge beneath northern Costa Rica. Previous 3-D tomography studies of Costa Rica suggested that the mantle wedge south of the Nicoya Peninsula was anhydrous, though central Costa Rica forearc mantle appeared hydrated (Husen *et al.* 2003a). The Nicoya Peninsula study region discussed here occurs predominantly northwest of and has greater depth resolution than the most recently calculated country-wide tomography study (Husen *et al.* 2003a); in particular, the forearc mantle wedge beneath the peninsula appears localized in a region of poor resolution in the country-wide model. In the Husen *et al.* (2003a) model, V_P ranged from 6.8 to 7.2 km s^{-1} in the forearc mantle with significant along-strike variability. This study indicates that low V_P values (7.0–7.6 km s^{-1}) vary little along-strike, suggesting fairly uniform hydration of the forearc mantle wedge.

The observed *P*-wave velocity reduction reported in this study corresponds to serpentinization of 20–25 per cent (Fig. 10) (i.e. Christensen 1966; Carlson & Miller 2003). Resolution modelling suggests anomaly recovery in the forearc mantle region of ∼65–70 per cent over the initial model. This implies V_P anomalies may be

underestimated and that the degree of serpentinization in the forearc wedge may be higher. The theoretical increase in V_P/V_S, which should push V_P/V_S over 1.80 throughout the wedge, is not observed, and ratios spatially vary from 1.70 to 1.80, or from anhydrous to 10 per cent serpentinization (Carlson & Miller 2003). Choice of V_P/V_S damping parameter additionally complicates the interpretation; tests using lower V_P/V_S damping lead to greater model variance and locally increased V_P/V_S amplitudes to >2.0.

7 CONCLUSIONS

The depth extent and width of the seismogenic zone illuminated by interseismic microseismicity varies along-strike of the Middle America subduction zone. Beneath the southern Nicoya Peninsula, interplate microseismicity extends from 12 km BSL, 70–75 km from the trench, to 26 km BSL, 100 km from the trench. In the northern Nicoya Peninsula, interplate seismicity extends from 17 to 28 km BSL, 75 to 88 km from the trench. The downdip limit of interplate microseismicity on the EPR crust occurs 12 km closer to the trench than it does on the CNS crust due to the steepening of the subducting plate. The updip extent is ∼5 km deeper north of the CNS–EPR plate suture. Along the suture both the updip and downdip extent of interplate microseismicity steps trenchward.

Geodetic modelling and interplate microseismicity provide apparently disparate spatial constraints on seismogenic zone updip and downdip limits (Norabuena *et al.* 2004; Schwartz & DeShon 2006; this study). The updip limit of interplate microseismicity is associated with the termination of anomalously low V_P along the plate interface and the 200–250°C isotherm estimates from thermal modelling. This change in velocity may represent a transition from ophiolitic Nicoya Complex to mid-crust compositions with increasing depth along the subduction thrust, while the onset of seismicity may be a mechanical effect of changing composition in the upper plate. Alternately, low V_P may indicate increased hydration in the upper and/or lower plates, and microseismicity may result due to changes in pore fluid pressure with increasing depth due to dehydration reactions within the subducting slab (Schwartz & DeShon 2006). The downdip edge of plate interface microseismicity neither directly correlates to the intersection of the continental Moho and oceanic crust nor to the modelled seaward extent of the brittle/ductile transition at 300–350°C. Low *P*-wave velocities in the mantle wedge indicate hydration and serpentinization of 15–25 per cent beneath the Nicoya Peninsula, allowing for a conditionally stable mantle wedge (DeShon & Schwartz 2004). Though the mantle wedge may rupture during large earthquakes, during the current interseismic period, the frictional stability state apparently does not allow microseismicity nucleation.

Multiple studies resulting from the CRSEIZE program, including the local earthquake tomography study presented here, have shown that interseismic microseismicity along the Nicoya Peninsula margin does not reflect the extent of the potential rupture area of subduction megathrust earthquakes. Hence, microseismicity may be a temporally variable feature within the earthquake cycle as loading increases along the plate interface, and, even when present, interplate microseismicity may not uniquely define the full seismogenic thrust interface. Although temperature may serve as a good proxy for defining the current seismogenic zone, deciding which isotherm describes the seismogenic zone over an entire seismic cycle is difficult; it may depend on the local subduction zone setting, and of course is affected by uncertainties in thermal models. As exemplified by the Costa Rica margin, the extent of locking along the subduction thrust, historic rupture dimension, temperature, hydration state and location of microseismicity must be used in combination to assess the potential for earthquake rupture along the subduction megathrust.

ACKNOWLEDGMENTS

We thank Alan Sauter and Sharon Escher for the OBS fieldwork and data processing components of this project, GEOMAR for the use of R/V *Sonne* cruise SO-144 leg 3b for OBS deployment, and the R/V *Reville* for OBS recovery. Some instruments used in the field program were provided by the PASSCAL facility of the Incorporated Research Institutions for Seismology (IRIS) through the PASSCAL Instrument Center at New Mexico Tech. Land data collected during this experiment are available through the IRIS Data Management Center, and OBS data are available by request through LMD at SIO. The facilities of the IRIS Consortium are supported by the National Science Foundation under Cooperative Agreement EAR-0004370. Figures made using GMT (Wessel & Smith 1998) and TOMO2GMT available through Stephan Husen. Constructive reviews by G. Laske, C. Thurber, S. Husen, and an anonymous reviewer significantly improved the manuscript. This work was supported by NSF grants OCE 9910609 and EAR0229876 to SYS, OCE9910350 to LMD and OCE 9905469 to THD.

REFERENCES

Aki, K. & Lee, W.H.K., 1976. Determination of three-dimensional anomalies under a seismic array using first P arrival times from local earthquakes, 1. A homogeneous initial model, *J. geophys. Res.,* **81,** 4381–4399.

Avants, M., Schwartz, S.Y., Newman, A.V. & DeShon, H.R., 2001. Large underthrusting earthquakes beneath the Nicoya Peninsula, *EOS Trans. Am. geophys. Un.,* **82,** F1266.

Barckhausen, U., Roeser, H.A. & von Huene, R., 1998. Magnetic signature of upper plate structures and subducting seamounts at the convergent margin off Costa Rica, *J. geophys. Res.,* **103,** 7079–7094.

Barckhausen, U., Ranero, C.R., von Huene, R., Cande, S.C. & Roeser, H.A., 2001. Revised tectonic boundaries in the Cocos Plate off Costa Rica: implications for the segmentation of the convergent margin and for plate tectonic models, *J. geophys. Res.,* **106,** 19 207–19 220.

Byrne, D.E., Davis, D.M. & Sykes, L.R., 1988. Loci and maximum size of thrust earthquakes and the mechanics of the shallow region of subduction zones, *Tectonics,* **7,** 833–857.

Carlson, R.L. & Miller, D.J., 2003. Mantle wedge water contents estimated from seismic velocities in partially serpentinized peridotites, *Geophys. Res. Lett.,* **30,** 1250, doi:10.1029/2002GL016600.

Christensen, N., 1966. Elasticity of ultrabasic rocks, *J. geophys. Res.,* **71,** 5921–5931.

Christeson, G.L., McIntosh, K.D., Shipley, T.H., Flueh, E.R. & Goedde, H., 1999. Structure of the Costa Rica convergent margin, offshore Nicoya Peninsula, *J. geophys. Res.,* **104,** 25 443–25 468.

Crosson, R.S., 1976. Crustal structure modeling of earthquake data, 1, simultaneous least squares estimation of hypocenter and velocity parameters, *J. geophys. Res.,* **8,** 3036–3046.

Currie, C.A., Hyndman, R.D., Wang, K. & Kostoglodov, V., 2002. Thermal models of the Mexico subduction zone: implications for the megathrust seismogenic zone, *J. geophys. Res.,* **107,** 2370, doi:10.1029/2001JB000886.

DeMets, C., 2001. A new estimate for present-day Cocos-Caribbean plate motion: implications for slip along the Central American volcanic arc, *Geophys. Res. Lett.,* **28,** 4043–4046.

DeShon, H.R., 2004. Seismogenic zone structure along the Middle America subduction zone, Costa Rica, *PhD thesis,* p. 356, University of California, Santa Cruz.

DeShon, H.R. & Schwartz, S.Y., 2004. Evidence for serpentinization of the forearc mantle wedge along the Nicoya Peninsula, Costa Rica, *Geophys. Res. Lett.,* **31,** L21611, doi:10.1029/2004GL021179.

DeShon, H.R., Schwartz, S.Y., Bilek, S.L., Dorman, L.M., Gonzalez, V., Protti, J.M., Flueh, E.R. & Dixon, T.H., 2003. Seismogenic zone structure of the southern Middle America Trench, Costa Rica, *J. geophys. Res.,* **108,** 2491, doi:10.1029/2002JB002294.

Eberhart-Phillips, D., 1986. Three-dimensional velocity structure in Northern California Coast Ranges from inversion of local earthquake arrival times, *Bull. seism. Soc. Am.,* **76,** 1025–1052.

Eberhart-Phillips, D., 1990. Three-dimensional *P* and *S* velocity structure in the Coalinga region, California, *J. geophys. Res.,* **95,** 15 343–15 363.

Eberhart-Phillips, D. & Reyners, M., 1997. Continental subduction and three-dimensional crustal structure: the northern South Island, New Zealand, *J. geophys. Res.,* **102,** 11 843–11 861.

Eberhart-Phillips, D. & Reyners, M., 1999. Plate interface properties in the Northeast Hikurangi subduction zone, New Zealand, from converted seismic waves, *Geophys. Res. Lett.,* **26,** 2565–2568.

Ellsworth, W.L., 1977. Three-dimensional structure of the crust and mantle beneath the island of Hawaii, *PhD thesis,* p. 327, Massachusetts Institute of Technology, Cambridge.

Evans, J.R., Eberhart-Phillips, D. & Thurber, C.H., 1994. User's manual for SIMULPS12 for imaging *Vp* and *Vp*/*Vs*: a derivative of the Thurber tomographic inversion SIMUL3 for local earthquakes and explosions. *U.S. Geol. Surv. Open-File Report*, 94–431, U.S. Government Printing Office.

Fisher, A.T., Stein, C.A., Harris, R.N., Wang, K., Silver, E.A., Pfender, M., Hutnak, M., Cherkaoui, A., Bodzin, R. & H. Villinger 2003. Abrupt thermal transition reveals hydrothermal boundary and role of seamounts within the Cocos Plate, *Geophys. Res. Letts.,* **30,** 1550, doi:10.1029/2002GL016766.

Güendel, F., 1986. Seismotectonics of Costa Rica: an analytical view of the southern terminus of the Middle America Trench, *PhD thesis,* p. 157, University of California, Santa Cruz.

Harris, R.N. & Wang, K., 2002. Thermal models of the Middle America trench at the Nicoya Peninsula, Costa Rica, *Geophys. Res. Lett.,* **29,** 2010, doi:10.1029/2002GL015406.

Haslinger, F. *et al.*, 1999. 3-D crustal structure from local earthquake tomography around Gulf of Arta (Ionian region), NW Greece, *Tectonophysics,* **304,** 210–218.

Husen, S., Kissling, E., Flueh, E. & Asch, G., 1999. Accurate hypocentre determination in the seismogenic zone of the subducting Nazca Plate in northern Chile using a combined on-/offshore network, *Geophys. J. Int.,* **138,** 687–701.

Husen, S., Kissling, E., & Flueh, E.R., 2000. Local earthquake tomography of shallow subduction in north Chile: a combined onshore and offshore study, *J. geophys. Res.,* **105,** 28 183–28 198.

Husen, S., Quintero, R., Kissling, E. & Hacker, B., 2003a. Subduction-zone structure and magmatic processes beneath Costa Rica constrained by local earthquake tomography and petrological modeling, *Geophys. J. Int.,* **155,** 11–32.

Husen S., Kissling, E., Deichmann, N., Wiemer, S., Giardini, D. & Baer, M., 2003b. Probabilistic earthquake location in complex three-dimensional velocity models: application to Switzerland, *J. geophys. Res.,* **108**(B2), 2077, doi:10.1029/2002JB001778.

Hutnak, M. *et al.*, 2006. The thermal station of 18–24 Ma upper lithosphere subducting below the Nicoya Peninsula, northern Costa Rica, in The Seismogenic Zone of Subduction Thrust Faults, eds Dixon, T.H. & Moore, J.C., Columbia University Press, New York, in press.

Hyndman, R.D. & Peacock, S.M., 2003. Serpentinization of the forearc mantle, *Earth planet. Sci. Lett.,* **212,** 417–432.

Hyndman, R.D. & Wang, K., 1993. Thermal constraints on the zone of major thrust earthquake failure—the Cascadia subduction zone, *J. geophys. Res.,* **98,** 2039–2060.

Hyndman, R.D., Yamano, M., & Oleskevich, D.A., 1997. The seismogenic zone of subduction thrust faults, *The Island Arc,* **6,** 244–260.

Iinuma, T. *et al.*, 2004. Inter-plate coupling in the Nicoya Peninsula, Costa Rica, as deduced from a trans-peninsula GPS experiment, *Eart. Plan. Sci. Lett.* **223,** 203–212.

Jacobson, R.S., Dorman, L.M., Purdy, G.M., Schultz, A. & Solomon, S.C., 1991. Ocean Bottom Seismometer facilities available, *EOS Trans. Am. Geophys. Un.,* **72,** 405–515.

Kimura, G., Silver, E.A. & Blum, P., 1997. *Proc. Ocean Drilling Program, Initial Reports* **170,** p. 458, Ocean Drill. Program, College Station, TX.

Kissling, E., Ellsworth, W.L. & Cockerham, R., 1984. Three-dimensional structure of the Long Valley Caldera, California, region by geotomography, *U.S. Geol. Surv. Open File Rep.*, 84–939, 188–220.

Kissling, E., Ellsworth, W.L., Eberhart-Phillips, D. & Kradolfer, U., 1994. Initial reference models in local earthquake tomography, *J. geophys. Res.,* **99,** 19 635–19 646.

Kissling, E., Kradolfer, U. & Maurer, H., 1995. VELEST user's guide-short introduction, *Institute of Geophysics and Swiss Seismological Service,* 25 pp, ETH, Zurich.

Kissling, E., Husen, S. & Haslinger, F., 2001. Model parameterization in seismic tomography: a choice of consequences for the solution quality, *Phys. Eart. planet. Int.,* **123,** 89–101.

Langseth, M.G. & Silver, E.A., 1996. The Nicoya convergent margin-a region of exceptionally low heat flow, *Geophys. Res. Lett.,* **23,** 891–894.

Lundgren, P., Protti, M., Donnellan, A., Heflin, M., Hernandez, E. & Jefferson, D., 1999. Seismic cycle and plate margin deformation in Costa Rica: GPS observations from 1994 to 1997, *J. geophys. Res.,* **104,** 28 915–28 926.

Marshall, J.S. & Anderson, R.S., 1995. Quaternary uplift and seismic cycle deformation, Peninsula de Nicoya, Costa Rica, *Geol. Soc. Am. Bull.,* **107,** 463–473.

Matumoto, T., Othake, M., Latham, G. & Umaña, J., 1977. Crustal structure of southern Central America, *Bull. seis. Soc. Am.,* **67,** 121–134.

Michelini, A. & McEvilly, T.V., 1991. Seismological studies at Parkfield: I. Simultaneous inversion for velocity structure and hypocenters using cubic b-splines parameterization, *Bull. seism. Soc. Am.,* **81,** 524–552.

Moore, J.C. & Saffer, D., 2001. Updip limit of the seismogenic zone beneath the accretionary prism of southwest Japan: an effect of diagenetic to low-grade metamorphic processes and increasing effective stress, *Geology,* **29,** 183–186.

Moore, J.C., Rowe, C. & Meneghini, F., 2006. How can accretionary prisms elucidate seismogenesis in subduction zones?, in The Seismogenic Zone of Subduction Thrust Faults, eds Dixon, T.H. & Moore, J.C., Columbia University Press, New York, in press.

Newman, A.V., Schwartz, S.Y., Gonzales, V., DeShon, H.R., Protti, J.M. & Dorman, L., 2002. Along strike variability in the seismogenic zone below Nicoya Peninsula, Costa Rica, *Geophys. Res. Lett.,* **29,** doi:10.1029/2002GL015409.

Norabuena, E. *et al.*, 2004. Geodetic and seismic constraints on some seismogenic zone processes in Costa Rica, *J. geophys. Res.,* **109,** B11403, doi:10.1029/2003JB002931.

Oleskevich, D.A., Hyndman, R.D. & Wang, K., 1999. The updip and downdip limits to great subduction earthquakes: thermal and structural models of Cascadia, south Alaska, SW Japan and Chile, *J. geophys. Res.,* **104,** 14 965–14 991.

Pacheco, J.F. & Sykes, L.R., 1992. Seismic moment catalog of large, shallow earthquakes, 1900–1989, *Bull. seism. Soc. Am.,* **82,** 1306–1349.

Pacheco, J.F., Sykes, L.R. & Scholz, C.H., 1993. Nature of seismic coupling along simple plate boundaries of the subduction type, *J. geophys. Res.,* **98,** 14 1333–14 159.

Peacock, S.M., van Keken, P.E., Holloway, S.D., Hacker, B.R., Abers, G.A. & Furgason, R.L., 2005. Thermal structure of the Costa Rica-Nicaragua subduction zone, *Phys. Eart. plan. Sci. Int.,* **149,** 187–200.

Protti, M., Güendel, F. & McNally, K., 1994. The geometry of the Wadati-Benioff zone under southern Central America and its tectonic significance: results from a high-resolution local seismographic network, *Phys. Earth planet. Int.,* **84,** 271–287.

Protti, M., Güendel, F. & McNally, K., 1995a. Correlation between the age of the subducting Cocos plate and the geometry of the Wadati-Benioff zone under Nicaragua and Costa Rica, in *Geologic and Tectonic Development of the Caribbean Plate Boundary in Southern Central America, Special Paper 295*, ed. Mann, P., GSA, Boulder, CO, 309–326.

Protti, M. *et al.*, 1995b. The March 25, 1990 ($M_W = 7.0$, $M_L = 6.8$), earthquake at the entrance of the Nicoya Gulf, Costa Rica: its prior activity, foreshocks, aftershocks, & triggered seismicity, *J. geophys. Res.,* **100,** 20 345–20 358.

Protti, M., Schwartz, S.Y. & Zandt, G., 1996. Simultaneous inversion for earthquake location and velocity structure beneath central Costa Rica, *Bull. seism. Soc. Am.,* **86,** 19–31.

Protti, M., Güendel, F. & Malavassi, E., 2001. *Evaluación del Potencial Sísmico de la Península de Nicoya*, Editorial Fundacion UNA, Heredia, Costa Rica, p. 144.

Quintero, R. & Güendel, F., 2000. Stress field in Costa Rica, Central America, *J. Seis.,* **4,** 297–319.

Quintero, R. & Kissling, E., 2001. An improved *P*-wave velocity reference model for Costa Rica, *Geofis. Int.,* **40,** 3–19.

Quintero, R. & Kulhanek, O., 1998. *Pn*-wave observations in Costa Rica, *Geofis. Int.,* **37**.

Ranero, C.R. & von Huene, R., 2000. Subduction erosion along the Middle America convergent margin, *Nature,* **404,** 748–752.

Ranero, C.R., Phipps Morgan, J., McIntosh, K. & Reichert, C., 2003. Bending-related faulting and mantle serpentinization at the Middle America trench, *Nature,* **425,** 367–373.

Reyners, M., Eberhart-Phillips, D. & Stuart, G., 1999. A three-dimensional image of shallow subduction: crustal structure of the Raukumara Peninsula, New Zealand, *Geophys. J. Int.,* **137,** 873–890.

Saffer, D.M. & Marone, C., 2003. Comparison of smectite- and illite-rich gouge frictional properties: application to the updip limit of the seismogenic zone along subduction megathrusts, *Earth planet. Sci. Lett.,* **215,** 219–235.

Sallarès, V., Dañobeitia, J.J., Flueh, E.R. & Leandro, G., 1999. Seismic velocity structure across the middle American landbridge in northern Costa Rica, *J. Geodyn.,* **27,** 327–344.

Sallarès, V., Dañobeitia, J.J. & Flueh, E.R., 2000. Seismic tomography with local earthquakes in Costa Rica, *Tectonophysics,* **296,** 61–78.

Sallarès, V., Dañobeitia, J.J. & Flueh, E.R., 2001. Lithospheric structure of the Costa Rican Isthmus: effects of subduction zone magmatism on an oceanic plateau, *J. geophys. Res.,* **106,** 621–643.

Sauter, A., Hallinan, J., Currier, R., Barash, T., Wooding, B., Schultz, A. & Dorman, L.M., 1990. A new ocean bottom seismometer, *Conference Proceedings on Marine Instrumentation, MPL-U-125/90*, Marine Technology Society, Columbia, MD, 99–104.

Schwartz, S.Y. & DeShon, H.R., 2006. Distinct Geodetic and Seismic Up-dip Limits to the Northern Costa Rica Seismogenic Zone: evidence for Two Mechanical Transitions, in The Seismogenic Zone of Subduction Thrust Faults, eds Dixon, T.H. & Moore, J.C., Columbia University Press, New York, in press.

Shipley, T.H., McIntosh, K.D., Silver, E.A. & Stoffa, P.L., 1992. Three-dimensional seismic imaging of the Costa Rica accretionary prism: structural diversity in a small volume of the lower slope, *J. geophys. Res.,* **97,** 4439–4459.

Smith, W.H.F, & Wessel, P., 1990. Gridding with continuous curvature splines in tension, *Geophysics,* **55,** 293–305.

Spinelli, G.A. & Saffer, D., 2004. Along-strike variations in underthrust sediment dewatering on the Nicoya margin, Costa Rica related to the updip limit of seismicity, *Geophys. Res. Lett.,* **31,** 4613, doi:10.1029/2003GL018863.

Spinelli, G.A. & Underwood, M.B., 2004. Characterization of sediment entering the Costa Rica subduction zone: implications for fluid partitioning along the Nicoya Peninsula plate interface, *Island Arc,* **3,** 432–451.

Stein, C.A. & Stein, S., 1992. A model for the global variation in oceanic depth and heat flow with lithospheric age, *Nature,* **359,** 123–129.

Thurber, C.H., 1981. Earth structure and earthquake locations in the Coyote Lake area, central California, *PhD thesis,* p. 339, Massachusetts Institute of Technology, Cambridge.

Thurber, C.H., 1983. Earthquake locations and three-dimensional crustal structure in the Coyote Lake area, central California, *J. geophys. Res.,* **88,** 8226–8236.

Thurber, C.H., 1992. Hypocenter-velocity structure coupling in local earthquake tomography, *Phys. Earth planet. Inter.,* **7,** 55–62.

Thurber, C.H., 1993. Local earthquake tomography: velocities and V_P/V_S theory, in *Seismic Tomography: Theory and Practice*, pp. 563–583, eds Iyer, H.M. & Hirahara, K., Chapman and Hall, London, United Kingdom.

Thurber, C. & Eberhart-Phillips, D., 1999. Local earthquake tomography with flexible gridding, *Computers and Geosciences,* **25,** 809–818.

Toomey, D.R. & Foulger, G.R., 1989. Tomographic inversion of local earthquake data from the Hengill-Grensdalur central volcano complex, Iceland, *J. geophys. Res.,* **94,** 17 497–17 510.

von Huene, R., Ranero, C.R., Weinrebe, W. & Hinz, K., 2000. Quaternary convergent margin tectonics of Costa Rica: segmentation of the Cocos Plate and Central American volcanism, *Tectonics,* **19,** 314–334.

von Huene, R., Ranero, C.R. & Vannucchi, P., 2004. A generic model of subduction erosion, *Geology,* **32,** doi:10.1130/G20563.1, 913–916.

Vrolijk, P., 1990. On the mechanical role of smectite in subduction zones, *Geology,* **18,** 703–707.

Wagner, L.S., Beck, S. & Zandt, G., 2005. Upper mantle structure in the south central Chilean subduction zone (30° to 36°S), *J. geophys. Res.,* **110,** B01308, doi:10.1029/2004JB003238.

Walther, C. & Flueh, E., 2002. Remnant of the ancient Farallon Plate breakup: a low-velocity body in the lower oceanic crust of Nicoya Peninsula, Costa Rica—evidence from-angle seismics, *Geophys. Res. Lett.,* **29,** 1939, doi:10.1029/2002GL015026.

Wessel, P. & Smith, W.H.F., 1998. New, improved version of the Generic Mapping Tools Released, *EOS Trans. Am. geophys. Un.,* **79,** 579.

Ye, S., Bialas, J., Flueh, E.R., Stavenhagen, A. & von Huene, R., 1996. Crustal structure of the Middle American Trench off Costa Rica from wide-angle seismic data, *Tectonics,* **15,** 1006–1021.